Mechanical properties of copper octet-truss nanolattices

ZeZhou He [a], FengChao Wang [a], YinBo Zhu [a], HengAn Wu [a,1,*], Harold S. Park [b,1,*]

[a] CAS Key Laboratory of Mechanical Behavior and Design of Materials, Department of Modern Mechanics, CAS Center for Excellence in Nanoscience, University of Science and Technology of China, Hefei, Anhui 230027, China
[b] Department of Mechanical Engineering, Boston University, Boston, Massachusetts 02215, USA

A B S T R A C T

We investigate the mechanical properties of copper (Cu) octet-truss nanolattices through a combination of classical molecular dynamics (MD) simulations and theoretical analysis. The MD simulations show that Cu nanolattices with high relative density are stronger than bulk Cu, while also achieving higher strength at a lower relative density as compared to Cu meso-lattices. We demonstrate that modifying the classical octet-truss lattice model by accounting for nodal volume and bending effects through the free body diagram method is critical to obtaining good agreement between the theoretical model and the MD simulations. In particular, we find that as the relative density increases, nodal volume is the key factor governing the stiffness scaling of the nanolattices, while bending dominates the strength scaling. Most surprisingly, our analytic modeling shows that surface effects have little influence on the stiffness and strength scaling of the nanolattices, even though the cross sectional sizes of the nanowires that act as the lattice struts are on the order of 6 nm or smaller. This is because, unlike for individual nanowires, the mechanical response of the nanowire struts that form the nanolattice structure is also a function of bending and nodal volume effects, all of which depend nonlinearly on the nanolattice relative density. Overall, these results imply that nanoscale architected materials can access a new regime of architected material performance by simultaneously achieving ultrahigh strength and low density.

© 2017 Elsevier Ltd. All rights reserved.

1. Introduction

Architected structural materials have been investigated both experimentally and theoretically for many years. This has provided a compelling approach to obtaining structures that are simultaneously lightweight and strong. Numerous studies on architected structural materials have shown that the strength and stiffness of cellular materials depends on their structural arrangement (Deshpande et al., 2001a; Fleck et al., 2010; Gibson and Ashby, 1999). Architected materials can deform by either bending or stretching of the individual elements, which is determined by the topology of the lattice and its nodal connectivity, and this bending or stretching behavior defines the deformation mechanisms of architected structural materials (Fleck et al., 2010). Three dimensional lattice structures with connectivity of $Z = 12$ at the nodes are stretching-dominated and structures with $6 \leq Z < 12$ are bending-dominated (Deshpande et al., 2001a) The deformation mechanism directly

---

* Corresponding author.
  E-mail addresses: wuha@ustc.edu.cn (H. Wu), parkhs@bu.edu (H.S. Park).
[1] The authors declare no competing financial interest.
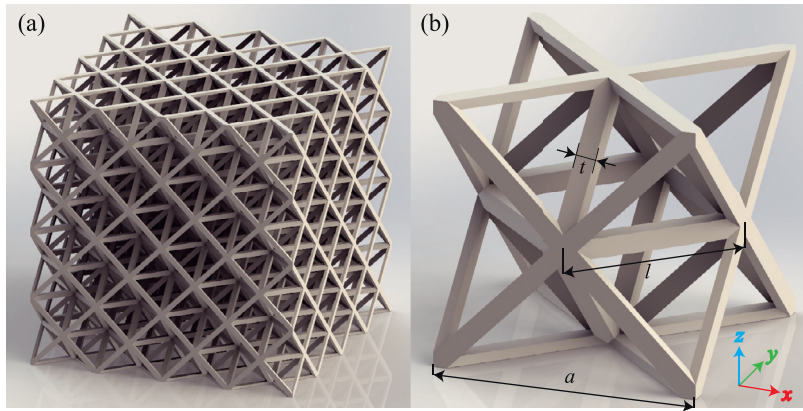
Fig. 1. (a) CAD image of the octet-truss lattice constructed by the 3D packing of unit cell. (b) A unit cell of the nanolattice and its geometric parameters studied in this paper.

impacts the effective properties of lattice structures, such as Young's modulus and yield strength (Fleck et al., 2010; Gibson and Ashby, 1999). The modulus and yield strength are also linked to the structure's relative density $\bar{\rho}$, which is defined as the ratio of the structure's volume within a unit cell and the volume of the unit cell (Gibson and Ashby, 1999). The yield strength and modulus of open-cell bending-dominated structures scale as $\sigma_y = 0.3\bar{\rho}^{1.5}\sigma_{ys}$ and $E = \bar{\rho}^2 E_s$, where σ_{ys} and E_s are the yield strength and modulus of the bulk material (Gibson and Ashby, 1999). For stretching-dominated structures, such as octet-truss lattice, the yield strength and modulus scale as $\sigma_y = 1/3\bar{\rho}\,\sigma_{ys}$ and $E = 1/9\bar{\rho}E_s$ (Deshpande et al., 2001b). Thus, the modulus and strength of stretching-dominated structures decreases more slowly than bending-dominated ones as the relative density decreases (Deshpande et al., 2001b; Fleck et al., 2010).

The strength and stiffness of macroscale architected structures depend as just discussed on their relative density and follow structural scaling laws (Gibson and Ashby, 1999). These scaling laws assume that the strength and stiffness of the constituent materials are constant. However, when the diameter of the individual structural elements decreases below the micron scale, many materials exhibit size effects, i.e. the well-known "smaller is stronger" effect in single crystalline metals (Greer and De Hosson, 2011; Jennings et al., 2010). As technology advances in fabrication methods, especially in 3D printing and nanofabrication, architected structural materials can be created with micro or even nanometer dimensions for the individual structural elements (Schaedler and Carter, 2016). Recent advances in additive manufacturing have also enabled the development of multiscale metallic metamaterials, which have feature sizes spanning seven orders of magnitude in length scale from tens of nanometers to centimeters, and which exhibit mechanical properties that are not attainable through the bulk material constituent (Zheng et al., 2016). The small sizes of these structural elements is important because these nano-materials often exhibit unique mechanical and physical properties not seen in the corresponding bulk materials (Bauer et al., 2016; Jang et al., 2013; Lee et al., 2015; Meza et al., 2015; Zheng et al., 2014, 2016). For example, metallic micro-lattices can recover under large compression strain and exhibit energy absorption capabilities similar to rubbery polymers like elastomers (Schaedler et al., 2011). Alumina ceramic nanolattices can recover up to 50% compressive strain while simultaneously being lightweight and ultra-strong (Meza et al., 2014). Cu meso-lattices composed of single crystal and nanotwinned structural elements have strength that is significantly enhanced relative to the equivalent bulk material (Gu and Greer, 2015). Both the ceramic nanolattices as well as Cu meso-lattices exhibit the "smaller is stronger" behavior due to size effects (Gu and Greer, 2015; Meza et al., 2014).

While the mechanical properties of nanolattices have been investigated recently, the size of the underlying structural elements has been on the order of a few hundred nanometers (Lee et al., 2015; Montemayor and Greer, 2015). Therefore, it is still unknown how surface effects, which become critical for sub-100 nm size scales, impact the mechanical properties of the nanolattices. At these size scales, surface effects, and not size effects, are the dominant operant physical mechanism, and it is currently unknown how the stiffening and strengthening that has been attributed to surface effects in individual nanowires (Park et al., 2009; Weinberger and Cai, 2012) impacts the mechanics of nanolattices.

The objective of this work is to explore the mechanical response of octet-truss nanolattices, illustrated in the CAD model depicted in Fig. 1, under uniaxial compression using classical molecular dynamics (MD) simulations. The nanolattices are constructed with single crystal FCC metal (Cu) nanowires as the individual structural element, and because the structures have a nodal connectivity of 12, its mechanical response is expected to be stretching-dominated (Deshpande et al., 2001b). In doing so, size effects which emerge from grain boundaries, nano-twins, Hall-Petch effects and which control the strengthening of meso-lattices (Gu and Greer, 2015), are not operant. Interestingly, we find that contrary to intuition, surface effects only weakly impact the Young's modulus and yield strength of the nanolattices. Instead, we find through analytic modeling that proper accounting of the nodal volume is the key factor governing the nanolattice stiffness, and the scaling of the stiffness, while the nanolattice strength and scaling of the strength are dominated by bending effects.
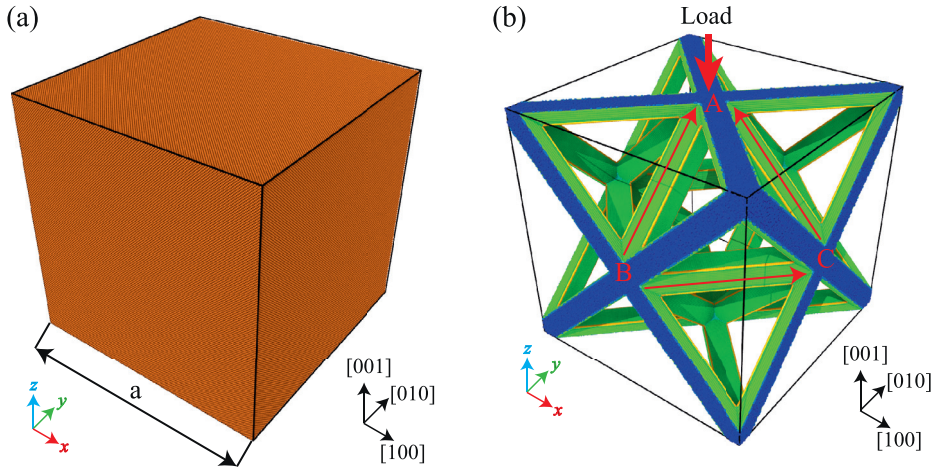
Fig. 2. (a) <100> crystal bulk. (b) Unit cell structure and crystal orientations of <100> nanolattices.

2. Simulation details

2.1. Molecular dynamics

In order to investigate the mechanical properties of nanolattices constructed with single crystal nanowires, we chose Cu square nanowires as the basic structural element, and MD simulations were performed using LAMMPS (Plimpton, 1995) with the embedded atom method (EAM) potential parametrized by Mishin et al. (2001). The Mishin potential has been shown to accurately capture both stacking fault and surface energies of Cu. In addition, analysis on stress-displacement, atomic relaxation and $\gamma - $ surface for {111}/<11$\bar{2}$> shear indicate that the Mishin Cu potential captures the essential deformation behavior in keeping with *ab initio* electronic structure calculations (Boyer et al., 2004).

To construct the MD models, we first used LAMMPS to generate a single crystal cubic bulk oriented in the <100> direction as shown in Fig. 2(a). Then, nanolattice ligaments were created by removing atoms from the bulk crystal, resulting in the nanolattices seen in Fig. 2(b). The crystal orientation of nanowires (or struts) in the nanolattice is different from the bulk as their axial orientations do not align with those of the unit cell. For nanolattices constructed from <100> crystal bulk, all of the struts (nanowires) are all along the <110> direction. In the following discussion, we refer to nanolattices created from <100> bulk as <100> nanolattices.

In this work, we performed MD simulations on a nanolattice unit cell with relative densities of about 4%~40%, which is defined as the ratio of the number of atoms in the nanolattice to the number in the bulk. The bulk cubic single crystals generated by LAMMPS had lengths of 30 and 40 nm, containing 2.4 million and 5.6 million atoms respectively. The resulting nanolattices contained between ~200,000 and 1.6 million atoms, with nanowire cross sectional lengths ranging from about 2–6 nm. Periodic boundary conditions were used in all three directions of the nanolattice unit cell. Starting with the initial temperature at 300 K, we performed simulations within the Isothermal-Isobaric (NPT) ensemble for 600 ps with a time step of 1 fs to let the system reach its equilibrium configuration. Then, deformation-controlled uniaxial compression with a strain rate of $10^9\,s^{-1}$ was applied along the z-direction of the unit cell for compressive strains up to 70%, while the pressure component perpendicular to the loading direction was controlled to maintain the uniaxial compression condition.

2.2. Relative density

A schematic model of the unit cell of the octet-truss nanolattice is shown in Fig. 1(b) together with the coordinate system. The relative density is computed by calculating the volumes of regions occupied by material in the CAD model, and scaling this by the unit cell volume, the octet-truss nanolattice relative density $\bar{\rho}$ is given by:

$$\bar{\rho} = 6\sqrt{2}\left(\frac{t}{l}\right)^2 - 3\left(2 + \sqrt{2}\right)\left(\frac{t}{l}\right)^3 \tag{1}$$

where t and l are the width and length of a strut defined in Fig. 1, respectively. It can be shown that Eq. (1) reduces to the relative density expression for an octet-truss lattice, if the node size is neglected (Deshpande et al., 2001b):

$$\bar{\rho} = 6\sqrt{2}\left(\frac{t}{l}\right)^2 \tag{2}$$

To simplify the volume calculation in MD simulations, bulk and surface atoms are viewed as having the same volume. The relative density of octet-truss nanolattices can be defined as the ratio of atoms' number in nanolattice and bulk, and
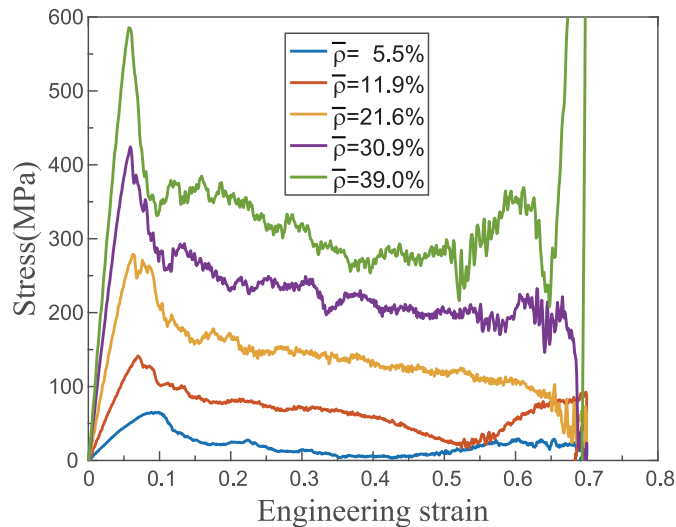
Fig. 3. Compressive stress-strain responses of <100> nanolattices with different relative densities.

its range is from 4.3% to 39.0%. The relative densities calculated by Eq. (1) range from 4.2% for the lowest density sample to 39.4% for the highest density sample, while relative densities calculated by Eq. (2) range from 5.0% for lowest density sample to 56.5% for the highest density sample. It is clear that neglecting the nodal volume leads to significantly larger relative densities for the high density lattice structures, thus demonstrating the relative accuracy of Eq. (1), which is used throughout this paper.

3. Compression of <100> nanolattices

3.1. Deformation mechanisms of <100> nanolattices

We now present MD simulations of the compression of nanolattices with different relative densities compressed to 70% strain, which as shown in Fig. 3 is the strain level at which the nanolattice fails and loses all load carrying capacity. The z-direction compressive stress-strain response for all nanolattices we considered, with relative densities from 5.5 to 39%, is shown in Fig. 3. While there are differences in response depending on the relative density, the mechanical response of the nanolattices does mimic the behavior previously seen in larger, bulk lattice structures. Specifically, an initial elastic region is first observed, where the stiffness increases with increasing relative density. This elastic region is followed by plastic yielding at compressive strains ranging from 5.8% to 8.8%. After yielding, a plateau in the flow stress is observed followed by failure via densification (Dong et al., 2015; Gibson and Ashby, 1999) in which the struts of the unit cells are pushed together, resulting in a sharp increase in the stress prior to failure (Gibson and Ashby, 1999).

To give further insights and to connect the atomic scale deformation mechanisms to the stress-strain response, we present in Fig. 4 the engineering stress-strain curves for the compression of <100> nanolattices with the relative density of ~5.5% and 39.0%. The aspect ratio of the struts (l/t) between relative densities of 5.5% and 39% decreases from 13 to 4. For the lowest relative density <100> nanolattices in Fig. 4(a), the process of compression can be divided into four stages, including elastic stage (I), plastic stage (II), plastic buckling (III) and densification stage (IV). Following the elastic stage (I), yielding occurs via nucleation of partial dislocations in the struts in stage (II). As the plastic strain increases, the struts exhibit plastic buckling, which leads to the significant decrease in flow stress in stage (III). Then, the opposing struts in nanolattices crush together due to structural buckling, which results in the stress increase in stage (IV) starting around 45% compressive strain.

In contrast, Fig. 4(b) shows that the nanolattices with the relative density of ~39.0% have a different stress-strain trend comparing to lower relative density. First, the yield strength is significantly elevated for the higher relative density, which is due to the larger volume of material that is present to resist the compressive loading. The process of deformation can be divided into three stages, containing elastic stage (I), plastic stage (II) as well as densification stage (III); buckling is not observed due to the small aspect ratios of the struts. The densification at larger relative density leads to a rapid increase in stress above the yield stress before failure, which occurs due to the larger amount of contact within the unit cell as compared to the lower relative density simulation.

We detail the evolution of plasticity in the <100> nanolattices in Fig. 5, where the atoms are highlighted by the centrosymmetry parameter (Kelchner et al., 1998) and visualized using the OVITO package (Stukowski, 2009). In the <100> nanolattices, all struts are along the <110> direction, and nanolattices with both low and high relative density exhibit similar deformation mechanisms. For the <110> nanowire orientation, it was previously shown that compressive deformation
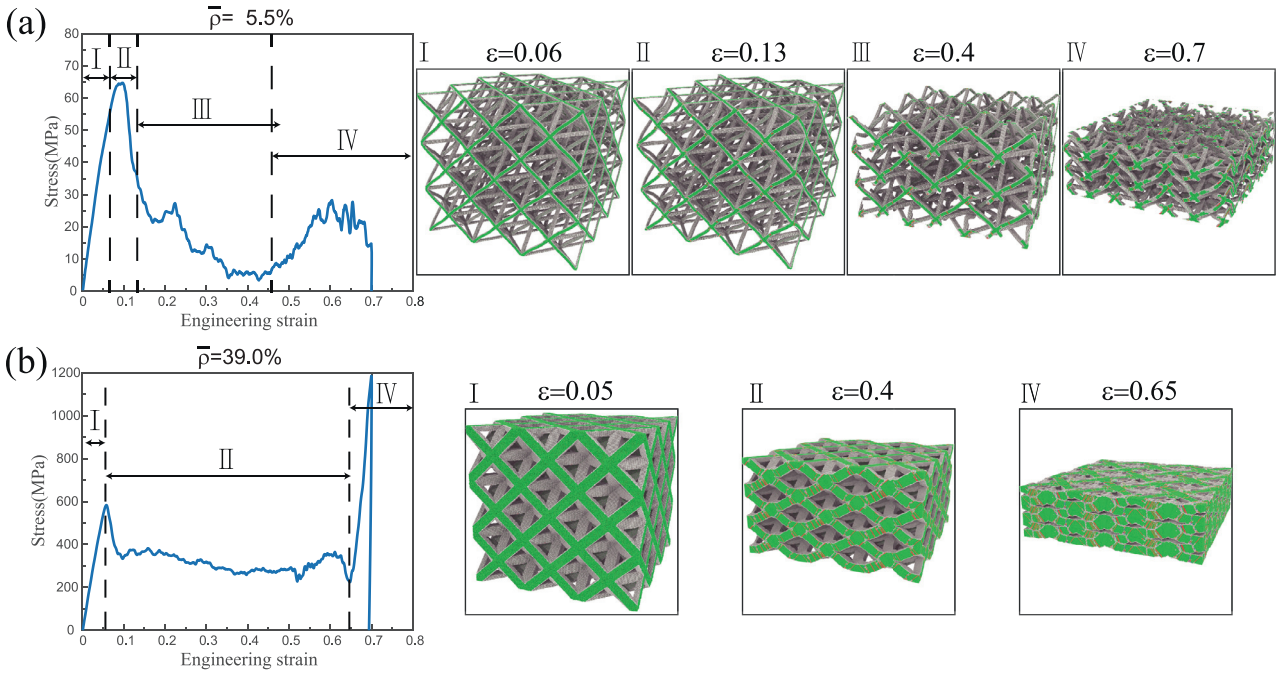
Fig. 4. Engineering stress-strain curve of <100> nanolattices with the relative density of (a) 5.5% and (b) 39.0%.
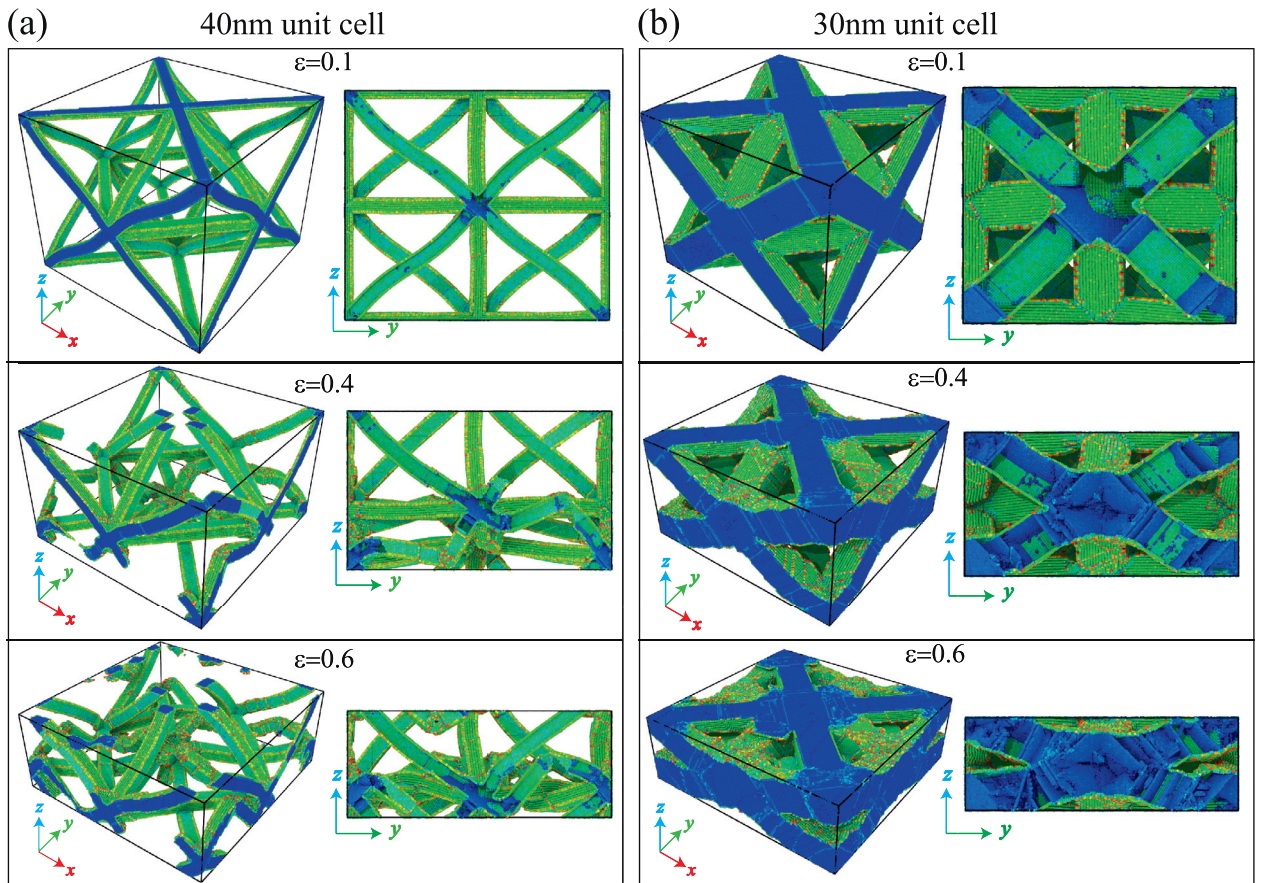
Fig. 5. Snapshots of <100> unit cells of nanolattices with $\bar{\rho} = 5.5\%$ (a) and $\bar{\rho} = 39.0\%$ (b) during compression. The development of plastic truss buckling in (a) can be seen as the total strain, ε, increases.

leads to plasticity via nucleation of both full and partial dislocations (Park et al., 2006). As is indicated in Fig. 5, partial dislocations of <100> nanolattices nucleate and propagate near the nodes during compression, which corresponds to strain bursts (Gu and Greer, 2015) and a drop in the flow stress. With the increase of strain ($\epsilon \sim 0.4$), we observe both full and partial dislocation generation near the nodes, along with surface steps, which causes strut buckling in the low relative density <100> nanolattices as shown in Fig. 5(a). At even larger compressive strains ($\epsilon \sim 0.6$), all struts in both nanolattices exhibit significant dislocation activity, while densification via strut contact occurs due to the large compressive strains that are applied.

4. Analytic modeling and discussion

In this section, we develop analytical models for the compressive response of nanolattices, while incorporating surface effects into the analytic models. The mechanical properties of octet-truss lattice material have been analyzed by Deshpande et al. (2001b). This model studied an ideal octahedral cell with cubic symmetry that assumed pin-joined struts, and the octahedral cells can be stacked to the octet-truss structure. It demonstrated that for small t/l, the contribution to stiffness and strength from the bending of the struts was negligible compared to from strut stretching (Deshpande et al., 2001a). The relative density $\bar{\rho}$ of the octet-truss lattice material is given by $\bar{\rho} = 6\sqrt{2}(t/l)^2$ (Deshpande et al., 2001b), where t and l are the width and length of a strut, respectively. As discussed previously around Eq. (2), this equation is a first order approximation and overestimates the relative density due to a double counting of the volume of the nodes. Under uniaxial compression, the stiffness and strength can be expressed as (Deshpande et al., 2001b):

$$E = \frac{2\sqrt{2}}{3}\left(\frac{t}{l}\right)^2 E_s \tag{3}$$

and

$$\sigma_y = 2\sqrt{2}\left(\frac{t}{l}\right)^2 \sigma_{ys} \tag{4}$$

where E_s and σ_{ys} are the orientation-dependent modulus and yield strength of each strut, where the struts in Cu <100> nanolattices are all along the <110> direction.

The ideal octet-truss lattice model works well for small t/l and relative densities, such that nodal volume and bending effects can be neglected when the relative density of the octet-truss lattice is smaller than about 10% (Dong et al., 2015; Gu and Greer, 2015). However, in this paper, the relative nanolattice densities range from 4 to 40%, which is larger than in previous studies. Moreover, when the regions surrounding the nodes are subject to complex stress states, the nodal volume and bending must be accounted for (Montemayor and Greer, 2015). The nodal volume was accounted for previously through the modification of the relative density in Eq. (1), though its effect on the strength and stiffness will be accounted for through the analytic models developed in this section. To account for both bending and nodal volume effects on the struts, we utilize the free body diagram method of Finnegan et al. (2007), which was recently used to predict the mechanical properties of Ti-6Al-4V octet-truss lattice structures (Dong et al., 2015). The corresponding free body diagram of octet-truss nanolattices is shown in Fig. 6(a) and (b).

4.1. Poisson effect

A key issue we consider in the analytic model is the elastic anisotropy of Cu. Because Cu exhibits significant elastic anisotropy, it is necessary to consider axial orientation effects on the elastic modulus of the struts (nanowires). The elastic modulus of each crystal is calculated for uniaxial loading in a given direction [$h\ k\ l$] by (Tschopp and McDowell, 2008):

$$\frac{1}{E_{[h\ k\ l]}} = S_{11} - (2S_{11} - 2S_{12} - S_{44})\frac{h^2k^2 + k^2l^2 + l^2h^2}{\left(h^2 + k^2 + l^2\right)^2} \tag{5}$$

where S_{ij} represents the elastic compliances for a given crystal, which were calculated from the elastic moduli C_{ij} given for the Cu EAM potential (Mishin et al., 2001).

From Fig. 2(b), the spatial direction of all struts in nanolattices can be divided into three directions, which are labeled as **AB, AC** and **BC**. For <100> nanolattices, struts **AB, AC** and **BC** are all oriented along the <110> direction. To facilitate the following analysis, we define modulus of struts **AB, AD, DF, BF** as E_1, struts **AC, AE, CF, EF** as E_2, and struts **BC, CD, BE, DE** as E_3, where $E_1 = E_2 = E_3 = E_{<110>} = 131.45$ GPa due to all struts being oriented along the <110> direction. According to free body diagram method, a strut of octahedral cell can be regarded as beam with length l and width t as shown in Fig. 6(b). During uniaxial compression, both ends of the strut are able to move because of the Poisson effect of the octahedral cell. Fig. 6(c) illustrates the deformation behavior of a doubly clamped beam when the octahedral cell is under uniaxial compression. By labeling the z-displacement as δ_z, the lateral (x)-displacement as δ_x and the lateral (y)-displacement as δ_y, the axial force F_A and shear force F_S in the strut are given by Timoshenko beam theory (Xia et al., 2011):

$$F_A = \frac{E_s A(\delta_z sin\theta - \delta_x cos\theta)}{l'} \tag{6}$$
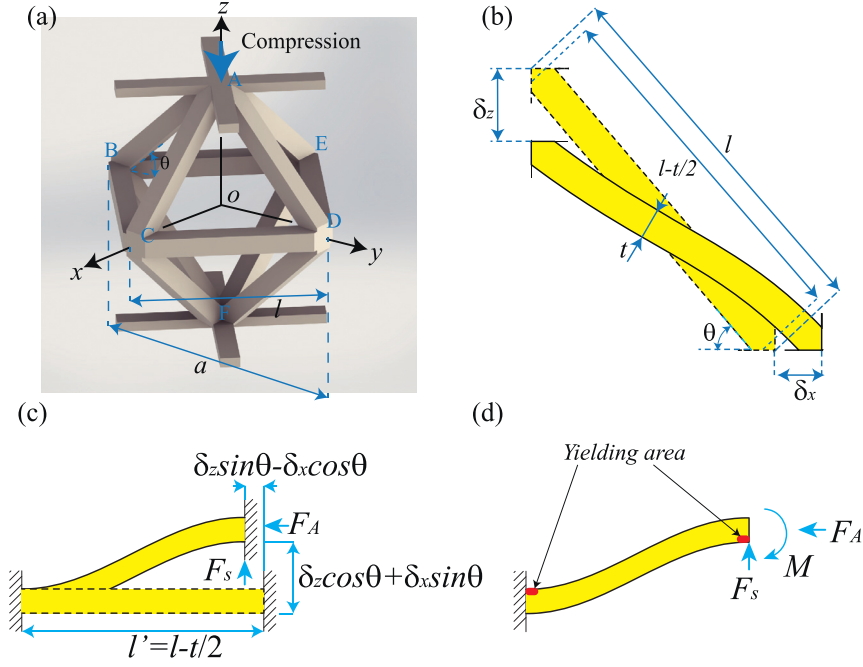
Fig. 6. Sketch of the deformation of a single out-of-plane strut under uniaxial compression. (a) Equivalent unit cell for nanolattices with the Cartesian coordinate system and loading direction also specified. (b), (c) Free body diagram for the strut when the unit cell is under uniaxial free compression. (d) Force analysis of the strut.

$$F_S = \frac{12K_T E_s I(\delta_z cos\theta + \delta_x sin\theta)}{l'^3} \tag{7}$$

where E_s is the Young's modulus of the strut along the loading direction, θ is strut inclined angle, A is the cross-sectional area, l' is the equivalent length of the strut, where $l - t \leq l' < l$ depending on the nodal volume of struts in nanolattices, I is the inertia moment of area of the beam cross section given by $I = t^4/12$ for square cross section of width t. $K_T = 1/(1 + 12E_s I/\kappa GAl'^2)$ is the shear modification of Timoshenko beam, where κ is the shear coefficient, G is the shear modulus. For a square beam, $\kappa = 5(1 + \nu)/(6 + 5\nu)$, where ν is the Poisson's ratio of Cu (Hutchinson, 2001). The total applied force F_b on a single strut in the z direction is expressed as

$$F_b = F_A sin\theta + F_S cos\theta \tag{8}$$

Because the shear force F_S to axial force F_A ratio scales as $(t/l')^2$, the contribution of struts' bending can be negligible if we ignore a second-order small quantity. If bending is neglected, we apply force equilibrium of octahedral unit cell along all three directions, and lateral displacements δ_x and δ_y are related to the vertical displacement δ_z by:

$$\delta_x = \frac{E_1(E_2 + E_3) - E_2 E_3}{E_1 E_2 + E_2 E_3 + E_3 E_1} \delta_z \tag{9a}$$

$$\delta_y = \frac{E_2(E_1 + E_3) - E_1 E_3}{E_1 E_2 + E_2 E_3 + E_3 E_1} \delta_z \tag{9b}$$

For <100> nanolattices, if we neglect surface effects, $E_1 = E_2 = E_3 = 131.45$ GPa, so $\delta_x = \delta_y = 1/3\delta_z$, which is the same with octet-truss lattice (Deshpande et al., 2001b; Dong et al., 2015). However, if $E_1 \neq E_2$, as could be caused by surface effects or elastic anisotropy, the lateral displacement δ_x and δ_y are not equal and the structure will deform differently compared to the macroscale octet-truss lattice.

4.2. Compressive stiffness

4.2.1. Compressive stiffness without surface effects

As is shown in Fig. 6(a), the external force F applied on the octahedral unit cell along z direction is equal to $4F_b$. The compressive stress σ_z is related to the force F_b and displacement δ_z via:

$$\sigma_z = \frac{4F_b}{l^2} = \frac{4\bar{E}t^2\delta_z}{3l'l^2} + \frac{2\sqrt{2}K_T(\lambda_1 + \lambda_2)\bar{E}t^4\delta_z}{3l'^3 l} \tag{10a}$$

where

$$\bar{E} = \frac{3E_1 E_2 E_3}{E_1 E_2 + E_2 E_3 + E_3 E_1} \tag{10b}$$

The strain ε_z applied to the octahedral cell is related to the displacement δ_z via:

$$\epsilon_z = \frac{2\delta_z}{a} = \frac{\sqrt{2}\delta_z}{l} \tag{11}$$

The effective Young's modulus E_z of the octahedral unit cell under uniaxial compression is then given by:

$$E_z = \frac{\sigma_z}{\epsilon_z} = \frac{2\sqrt{2}}{3}\bar{E}\left(\frac{t}{l}\right)^2 K_V^E K_B^E \tag{12a}$$

where

$$K_V^E = 1 + \frac{l - l'}{l'} \tag{12b}$$

$$K_B^E = 1 + K_T(\lambda_1 + \lambda_2)\left(\frac{t}{l'}\right)^2 \tag{12c}$$

where l' is the equivalent beam length, which is related to the width of struts in octahedral unit cell, and $\lambda_1 = E_1(1/E_2 + 1/E_3)/2$, $\lambda_2 = E_2(1/E_1 + 1/E_3)/2$. Consider the strut stretched in Fig. 6(b) and the corresponding representative beam shown in Fig. 6(c), and the equivalent length of the strut is given by $l' = l - t/2$ (Moongkhamklang et al., 2010). Comparing Eqs. (3) and (10b), $\bar{E}$ in Eq. (10b) is different from the modulus E_s of the bulk material, due to the explicit incorporation of crystal orientation effects.

We note that K_V^E and K_B^E are the modification of nodal volume and bending effect, respectively; these modifications can be neglected by setting $K_V^E = K_B^E = 1$. The nodal volume modification is purely geometric, whereas the bending effect depends explicitly on the elastic anisotropy of the nanolattice struts. It is clear that $K_B^E > 1$, which implies that accounting for bending will always increase E_z. It is also clear that $K_V^E > 1$, which again will lead to an increase in E_z compared to the octet-truss model. As is expressed in Eq. (12b) and (c), nodal volume and bending effects are first- and second-order quantities as compared with the compressive stress, respectively. If the relative densities of nanolattices are less than 1%, which means l/t is higher than 25, modifications of nodal volume and bending are given by $K_V^E \approx 1$ and $K_B^E \approx 1$, which means ideal octet-truss lattice works well for small relative densities. Based on these mathematical analyses, the octet-truss model is valid for low relative densities, while nodal volume and bending corrections must be considered if the relative density is greater than 1%.

4.2.2. Surface effects on elastic properties

Up to this point, we have not considered surface effects on the elastic properties of the nanolattice struts, i.e. in Eqs. (6) and (7). Thus, Eq. (12) does not contain surface effects, and all elastic stiffnesses should be modified if surface effects are operant, as for our small cross section nanowire struts. In the past 15 years, many theories have been developed to describe surface effects on the mechanical properties of nanomaterials (Dingreville and Qu, 2005; Miller and Shenoy, 2000). For the nanolattices, the octahedral unit cell is a stretching-dominated structure, which suggests that the individual nanowires can be modeled as undergoing axial compression. Perhaps the simplest form for capturing surface effects on the stiffness can be written as (Miller and Shenoy, 2000): $E^* = E_s + 4S_E t^{-1}$, where S_E is the surface modulus of nanowires, and E_s is the Young's modulus of the bulk material.

For the bending effect of nanowires, Feng *et al.* demonstrated that the residual surface stresses can be neglected because its influence on the effective modulus is much weaker than that of surface elasticity (Feng et al., 2009; He and Lilley, 2008). Surface elasticity on flexural stiffness can be given by (Feng et al., 2009; Miller and Shenoy, 2000): $(EI)^* = (E_s + 8S_E t^{-1})t^4/12$. Thus, λ_1 and λ_2 in Eq. (13) should be modified as: $\lambda_1^* = \lambda_1(1 + 8S_E/E_1 t)/(1 + 4S_E/E_1 t)$ and $\lambda_2^* = \lambda_2(1 + 8S_E/E_2 t)/(1 + 4S_E/E_2 t)$. These expressions can then directly be used to account for surface effects on the Young's modulus of the octahedral unit cell in Eq. (12).

4.2.3. Discussion

To compare the theoretical analysis and MD simulation results, the Young's modulus as a function of relative density is shown in Fig. 7. Here, the Young's modulus of the nanolattices was obtained by taking the slope of the linear elastic portion of the stress-strain response. Fitting the MD simulations by the functional form $E_z \propto E_s \bar{\rho}^n$ (Fleck et al., 2010; Gibson and Ashby, 1999), we obtain a value for the exponent $n = 1.23$, which is slightly higher than ideal octet-truss lattice ($n = 1$) (Deshpande et al., 2001b) and solid HDDA ($n = 1.1$) (Zheng et al., 2014), but lower than bending-dominated structures ($n = 2$) (Fleck et al., 2010; Gibson and Ashby, 1999) and hollow-tube alumina nanolattices ($n = 1.61$) (Meza et al., 2014). From Eq. (12b) and (c), we can find that the exponent n is mainly impacted by effects of nodal volume, with bending of secondary importance, which explains why the scaling of the Young's modulus is closer to the stretching-limit of $n = 1$.

To distinguish between bending, nodal volume and surface effects, Fig. 7 shows octet-truss lattice and five modified models in comparison with the MD simulation results. Table 1 lists the differences between these five models. The Young's
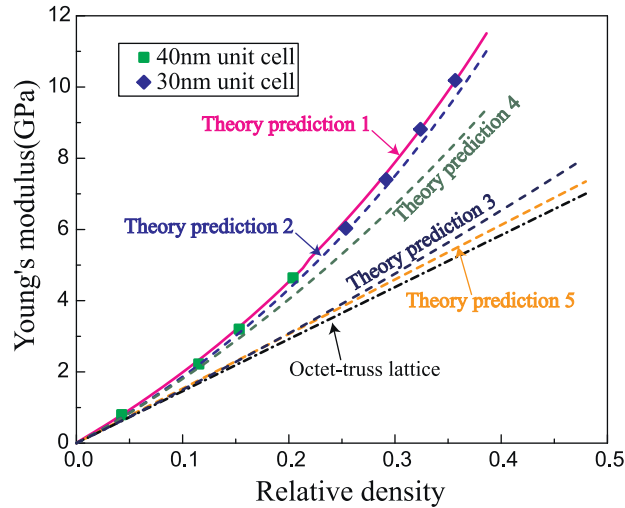
Fig. 7. Comparisons between the simulations and model predicted Young's modulus E_z as a function of relative density $\bar{\rho}$. MD simulation results and theory prediction expressed in Eq. (12) are plotted together in this figure. The differences of theory prediction 1~5 are listed in Table 1. Octet-truss lattice model is also drawn using Eq. (3).

Table 1
Differences of five theory predictions. "Yes" means this factor is included in this theory prediction, and "No" means this factor is not contained.

Theory predictions	Bending	Nodal volume	Surface effects
1	Yes	Yes	Yes
2	Yes	Yes	No
3	Yes	No	No
4	No	Yes	No
5	No	No	Yes

Table 2
Relevant parameters of single crystal bulk of copper (Meyers and Chawla, 2009; Mishin et al., 2001).

Crystal orientation	Young's Modulus (GPa)	Shear modulus (GPa)	Poisson's ratio
<100>	67.1	76.2	0.42
<110>	131.4	23.6	

Table 3
Relevant parameters of surface in crystalline. Surface modulus is calculated by MD simulations, and surface stress τ_0 is taken from (Sun et al., 2008).

Surface (hkl)	Orientation	Surface modulus (N/m)	Surface stress (N/m)
{1 0 0}	<100>		1.5157
{1 1 0}	<100>	30.61	1.1919
	<110>	−10.66	1.3793

modulus of single-crystalline bulk Cu along the <110> orientation is taken as 131.45 GPa (Tschopp and McDowell, 2008). In <100> nanolattices, all <110> struts have two {1 0 0} side surfaces and two {110} side surfaces. Based on the method of Shenoy's atomistic simulations, MD simulations using Mishin potential estimated the surface modulus of <110> single-crystalline Cu as $S_{E1} = 30.61 N/m$ on the (010) crystal surface and $S_{E2} = −10.66 N/m$ on the (10$\bar{1}$) surface (Shenoy, 2005). Tables 2 and 3 provides relevant mechanical properties of single crystal Cu in the <100> and <110> directions according to the Mishin potential.

Fig. 7 reveals that Eq. (12), which accounts for bending and nodal volume, agrees with the MD simulations. However, the classical octet-truss model, which neglects bending and nodal volume effects, shows increasing error compared to the MD simulation results as the relative density increases. Performing the five theory predictions enables us to demonstrate that accounting for nodal volume is the most important theoretical enhancement, followed by bending, and finally surface effects.

A natural question arises: what mechanism makes nodal volume and bending significant for nanolattices compared with previously studied macroscale octet-truss lattice systems, i.e. the ideal octet-truss lattices of Deshpande et al. (2001b), and Ti-6Al-4V octet-truss lattices (Dong et al., 2015)? And, why are surface effects relatively unimportant for nanolattices even though the strut widths (2–6 nm) lie solidly within the expected regime where surface effects are known to strongly impact their mechanical properties (Liang et al., 2005; Park et al., 2009; Park and Klein, 2008)?

In the analysis of ideal octet-truss lattice, truss elements are slender, and the nodal connectivity is assumed to be pin-jointed, so nodal volume and bending, which scales as $(t/l)^2$, are negligible (Deshpande et al., 2001a). For Ti-6Al-4V octet-truss lattices, their relative densities are between 2.4% and 15.9%, so the modification of nodal volume is taken into account for the relative density calculations. Furthermore, the nodal connectivity is pin-jointed for Ti-6Al-4V lattices, which cannot support a bending moment; this decreases the effect of bending during deformation (Dong et al., 2015). However, the Cu nanolattices studied here are single crystalline and have smaller aspect ratio struts (between 4 and 13) but larger relative density (between 4% and 40%), so nodal connectivity can be treated as rigid-jointed, which enhances the effect of bending. Moreover, the aspect ratio of the struts within the nanolattices is small compared with previously studied octet-truss lattices, so the effects of nodal volume and bending are enhanced in the nanolattices.

To explain why surface effects do not strongly impact the nanolattice elastic modulus, we calculate the difference between the modulus of the nanolattice with and without surface effects as $\Delta = E_z^* - E_z \approx 1.05\bar{\rho}^{1.23} \, S_E t^{-1}$, where E_z^* is the nanolattice stiffness with surface effects and E_z is the nanolattice stiffness neglecting surface effects. This difference demonstrates that nanolattices have lower free surface to volume ratio in unit cell (the order of $\bar{\rho}^{1.23}/t$) compared with an individual nanowire (the order of $1/t$) (Miller and Shenoy, 2000). For the strut widths in our work, which range from 2.1 to 6.0 nm, the difference is 0.1 GPa for the smallest relative density of $\bar{\rho} = 0.043$ and 0.61 GPa for the largest relative density of $\bar{\rho} = 0.4$. Given that the nanolattice stiffness is calculated from the MD simulations to be 0.797 GPa at the smallest relative density and 11.8 GPa at the largest, the error from neglecting surface effects is largest ($\sim$14%) for the smallest relative density, and decreasing to $\sim$5% for the largest relative density nanolattice we considered. Given that the classical octet-truss model predicts a nanolattice stiffness of 8.64 GPa at the highest relative density of $\bar{\rho} = 0.4$, for an error of 26.8%.

The impact of surface effects can also be interpreted using Fig. 8, where the dashed lines represent the Young's modulus as function of strut width with different relative densities, and the solid lines show the Young's modulus varying with length of unit cell. For each relative density (dashed lines), surface effects increase with decreasing strut width, which is consistent with size-dependent stiffening previously predicted for <110> FCC metal nanowires (Liang et al., 2005). Furthermore, for each unit cell length, as the relative density (or strut width) increases, surface effects tend to decrease. Finally, as the strut length, *a* increases, surface effects have decreasing impact. All of these trends are consistent to above analysis. It is clear that, particularly at the highest relative densities, surface effects play a very minor role in explaining the difference between the MD simulation results and the classical octet-truss solution.

4.3. Compressive strength

4.3.1. Elastic buckling

A stretching-dominated lattice structure may fail under compressive loading by elastic buckling or by plastic yielding depending on the aspect ratio (l/t) of the struts. At low relative densities, struts are flexible enough to collapse by elastic buckling before plastic yielding. The elastic buckling stress including surface effects is given by (Wang and Feng, 2009):

$$\sigma_E = \frac{n^2\pi^2(E_sI)^*}{Al'^2} + \frac{2\tau_0 t}{A} = \frac{n^2\pi^2}{12}E_s\left[1 + \frac{8S_E}{E_st} + \frac{24}{n^2\pi^2}\left(\frac{l}{t}\right)^2\left(\frac{\tau_0}{E_st}\right)\right]\left(\frac{t}{l}\right)^2\left(1 + \frac{l-l'}{l'}\right)^2 \tag{13}$$

where A is the strut cross-section area given by $A = t^2$, and E_s is equal to $max[E_1, E_2]$. The factor n is determined by the end conditions on the buckling struts. We simplify the problem by assuming that the struts are fixed at both ends. Thus, the rotational stiffness of the nodes is zero and $n = 2$ (Deshpande et al., 2001b). In the case of failure via elastic buckling:

$$\sigma_z^E = \frac{2\sqrt{2}}{3}\pi^2E_s\left[1 + \frac{8S_E}{E_st} + \frac{6}{\pi^2}\left(\frac{l}{t}\right)^2\left(\frac{\tau_0}{E_st}\right)\right]\left(\frac{t}{l}\right)^4\left(1 + \frac{l-l'}{l'}\right)^2 \tag{14}$$

For the lowest relative density (4.3%) simulated in this paper, the strut length and width of strut are 2.1 nm and 28.3 nm, respectively. According to Eq. (14), the elastic buckling stress of the nanolattices is 55.5 MPa, which is slightly higher than the yield strength (45.6 MPa) of nanolattices, so elastic buckling is not observed in this work. However, if surface effects are neglected, the buckling stress is lower than the yield strength, and nanolattices exhibit elastic buckling. Therefore, surface effects enhance the rigidity of the struts, which improves the stability of nanolattices with low relative density.

4.3.2. Yield strength

At high relative densities, l tends towards t, and a lattice structure will fail by yielding of the low aspect ratio struts. As shown in Fig. 6(d), if we remove the clamped constraint at one end of the beam, the equilibrium deformation of struts under uniaxial compression can be replaced by constraint reaction forces. Because struts in nanolattices are rigid-jointed,
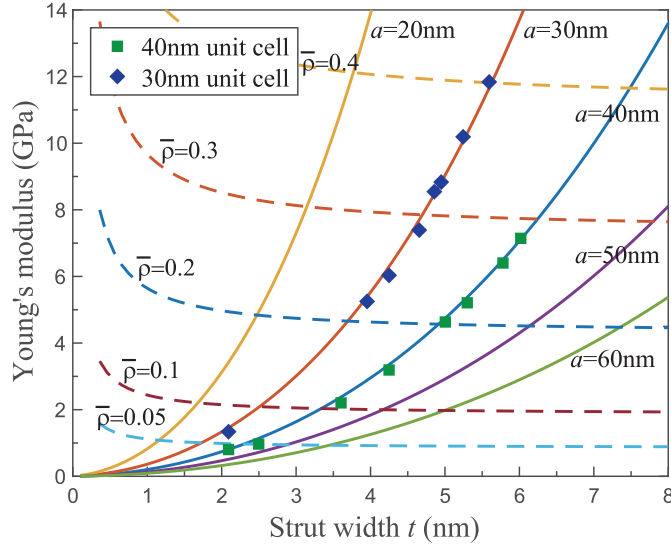
Fig. 8. Young's modulus of nanolattices as a function of strut width (dashed lines) and length of unit cell (solid lines) from theory prediction 1 and MD simulations (solid points).

the bending moment at both clamped boundary cannot be neglected. From Timoshenko beam theory, we can conclude the equilibrium moment is expressed as:

$$M = \frac{1}{2}F_S l' \tag{15}$$

The maximum normal stress in struts is given by:

$$\sigma_m = \frac{F_A}{A} + \frac{Mt}{2I} = \sigma_A \left[1 + 6\lambda \left(\frac{t}{l'} \right) \right] \tag{16a}$$

and

$$\sigma_A = \frac{F_A}{A} = \frac{\sqrt{2}}{3} \bar{E} \frac{\delta_z}{l'} \tag{16b}$$

where λ is equal to $max[\lambda_1, \lambda_2]$. The maximum normal stress in beam is at the clamped ends, which means the collapse of struts always occurs at clamped ends as is indicated in Fig. 6(d). This also corresponds to the MD simulations where plastic deformation originates at or near the nodes in the nanolattices, as shown in Fig. 9(b), which shows the von Mises stress distribution calculated from six components of virial stress of each atom (Zhou, 2003).

The maximum shear stress in struts is given by (Timoshenko and Goodier, 1970): $\tau_m = 3(1 + \chi)F_s/2t^2$, where χ is a constant depending on the cross sectional geometry and Poisson's ratio. Combining Eqs. (7) and (9), the maximum shear stress can be expressed as: $\tau_m = 3(1 + \chi)\lambda(t/l')^2\sigma_A$. This equation demonstrates that τ_m is a second order small quantity compared with the axial stress. In addition, the MD simulations show that dislocations nucleate from the surfaces of the struts at the nodes, while the maximum shear stress occurs at the neutral axis of the struts, or away from the surfaces (Timoshenko and Goodier, 1970), as showed in Fig. 9(c) and (d). For both of these reasons, shear stresses have little influence on dislocation nucleation in struts and are neglected in the following discussion.

Combining Eqs. (10) and (16), the stress applied to the octahedral unit cell σ_z can be expressed in terms of the axial stress σ_A in the strut:

$$\sigma_z = \frac{2\sqrt{2}t^2}{l^2}\sigma_A + \frac{2\sqrt{2}K_T(\lambda_1 + \lambda_2)t^4}{l'^2 l^2}\sigma_A \tag{17}$$

The yielding condition of strut can be effectively predicted by the von Mises criterion: $\sigma_v = \sigma_m$, where σ_v is the von Mises stress at yielding. As the loading increases, the von Mises stress gradually reaches its yield strength σ_{ys}. Therefore, the lattice strength is expressed as:

$$\sigma_y = 2\sqrt{2}\left(\frac{t}{l}\right)^2 \sigma_{ys} K_V^Y K_B^Y \tag{18a}$$

and

$$K_B^Y = \frac{1 + K_T(\lambda_1 + \lambda_2)\left(\frac{t}{l'}\right)^2}{1 + 6\lambda\left(\frac{t}{l'}\right)} \tag{18b}$$
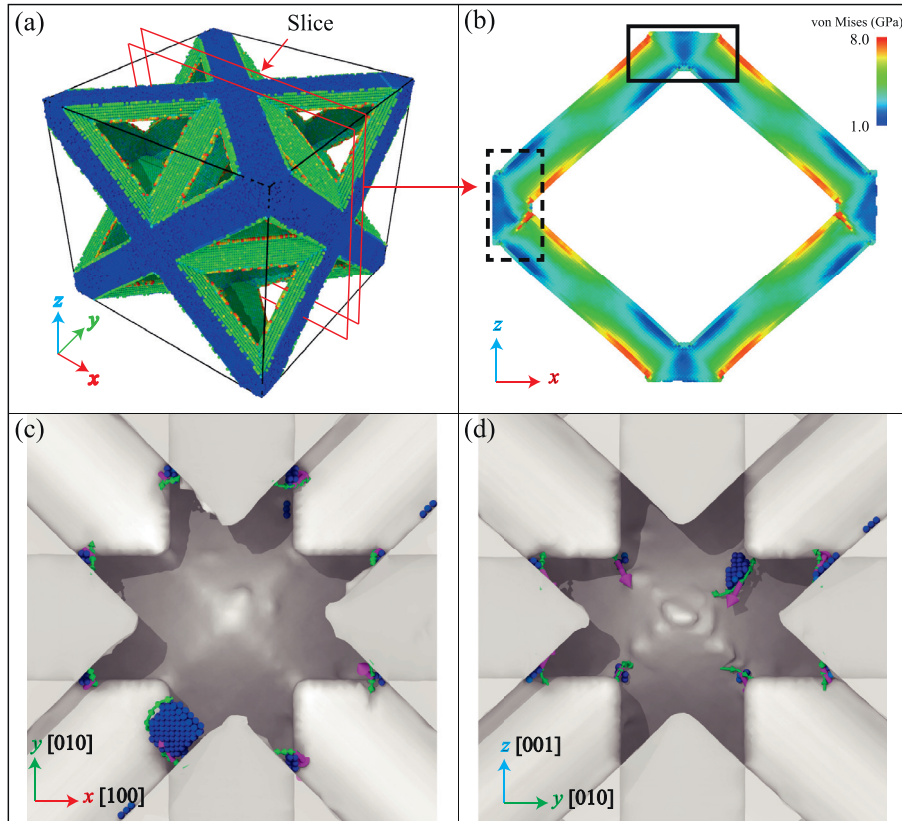
Fig. 9. Generation and propagation of partial dislocations at nodes of nanolattices during compression. (b) Schematic diagram of stress distribution. The red areas indicate yielding areas and are marked by box. (c), (d) Dislocation distribution of zoom areas signed by solid and dashed box, respectively. The green lines in (c) and (d) represent 1/6<112> dislocation, and the purple arrows are Burgers vector of dislocation (Stukowski et al., 2012). The white surface represents the surface of nanolattices. (For interpretation of the references to colour in this figure legend, the reader is referred to the web version of this article.)

K_V^Y and K_B^Y are the modification of nodal volume and bending effect, respectively. In Eq. (17), the modification of equivalent length is offset by the axial stress expressed in Eq. (16b). Therefore, different from Eq. (12b), K_V^Y in Eq. (18a) is always given by: $K_V^Y = 1$.

The strut bending effects on the yield strength are shown in Eq. (18b), which is a first order quantity compared with axial stress. An important difference in the bending effects on yield strength as compared to stiffness in Eq. (12c) is that the denominator of Eq. (18b) is always greater than 1, which is caused by moments at both end of the struts shown in Fig. 6(d) and expressed by Eq. (16). Therefore, $K_B^Y < 1$, which implies that bending always decreases σ_y. Similarly, if the relative densities are less than 1%, the bending effect modification is given by $K_B^Y \approx 1$, and the yield strength of nanolattices reduces to those of the ideal octet-truss lattice (Deshpande et al., 2001b).

4.3.3. Surface effects on yield strength of struts

So far, surface effects on the yield strength σ_{ys} of struts has not been considered in discussing the yielding of nanolattices. Numerous studies have demonstrated that yield strength of FCC metal nanowires depends on the orientation and size of the nanowires (Cao and Ma, 2008; Diao et al., 2004; Park et al., 2006). The yield stress varies with nanowire width t, and a behavior of the form $\sigma_{ys} = \sigma_{ys}^0 + Kt^{-1}$ is often observed, where σ_{ys}^0 and K are independent of t (Yang et al., 2009; Zhang et al., 2008). To determine the parameters in this equation, MD simulations using Mishin potential were performed to estimate the yield strength of <110> nanowires with different width (Park et al., 2006). Fitting the data from MD simulations, we obtain $\sigma_{ys}^0 = 9.48$ GPa and $K = 9.48$ N/m. This expressions can then directly be applied to account for surface effects on the yield strength of the octahedral unit cell in Eq. (18) (Hodge et al., 2007).

4.3.4. Discussion

The yield point was chosen as the stress at the first peak after the linear elastic loading region. The yield strengths of the nanolattices are plotted as a function of relative density in Fig. 10 with unit cell size of 40 nm for strut size of 2.2–6 nm, and unit cell size of 30 nm for strut size of 4.3–5.6 nm. As is shown in Fig. 10, size-dependent strengthening is revealed by comparing the nanolattice yield strength against the bulk yield strength. In the paper of Gu and Greer (2015), bulk
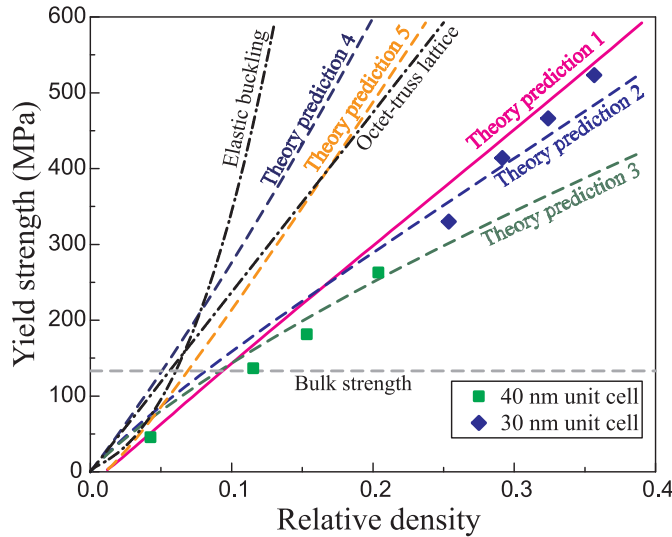
Fig. 10. Comparisons between the simulations and model predicated yield strength σ_y as a function of relative density $\bar{\rho}$. MD simulation results and theory prediction expressed in Eq. (18) are plotted together in this figure. The differences of theory prediction 1~5 are listed in Table 1. Octet-truss lattice model is also drawn using Eq. (4).

yield strength of Cu was calculated to be 133 MPa, and the maximum yield strength of meso-lattices is about 332 MPa with relative density of 0.8 (Gu and Greer, 2015). For <100> nanolattices, the maximum yield strength is about 586 MPa with relative density of 0.39. As shown in Fig. 12, comparison of the yield strengths of the nanolattices and the electroplated Cu thin film reveals that nanolattices with $\bar{\rho} > 0.1$ are stronger than the bulk, with the high-density <100> nanolattices ($\bar{\rho} \sim 0.26$) having the same strength as the densest meso-lattices ($\bar{\rho} \sim 0.8$) that were studied experimentally (Gu and Greer, 2015).

In comparing the MD results for yield strength with the analytic theory predictions summarized in Table 1, we find that bending is the key contributor to enable the octet truss model to match the MD simulation results. Specifically, the bending term shifts the octet truss yield stress curve down as compared to the octet truss result in Fig. 10 because bending is a first order effect that scales as t/l' according to Eq. (16). The yield strength of struts not considering surface effects is 7.11 GPa, which is the compressive strength of <110> nanowires with width of 4 nm (the median width of struts).

While bending alone leads to a slight underprediction of the yield strength, additionally incorporating nodal volume effects (theory prediction 2 in Fig. 10) shifts the yield stress curve up close to the MD results. A detailed analysis demonstrates that, however, theory prediction 2, which accounts for both bending and nodal volume, deviates from the MD yield stress curve at low relative densities, or equivalently struts with small widths. This is due to the size-dependent compressive strength of <110> nanowires, which increases with increasing nanowire width; as discussed with regards to the nanolattice modulus, surface effects had the largest effect on the low relative density nanolattices, which also manifests itself here with regards to the yield strength, as shown in Fig. 11. By incorporating surface effects in conjunction with bending and nodal volume via theory prediction 1, we are able to find good agreement with the MD simulations in Figs. 10 and 11. Thus, bending, surface effects and nodal volume contribute in decreasing order to the strength of nanolattices.

A further refinement in the ranges that the various mechanisms (bending, nodal volume, surface effects) dominate can be obtained by considering different nanolattice relative densities, as seen in Fig. 10. For low relative densities (under 5.5%), surface effects have a significant effect on the yield strength, due to the fact that the effects of bending and nodal volume are small as shown in Eq. (18), which can be simplified as: $K_B^Y \approx 1$ in the case of very small t/l (or very low relative density). This can also be observed in comparing theory predictions 1 and 2 in Fig. 10, where for low relative densities theory prediction 1, which includes surface effects, better matches the MD simulation results.

As the relative density increases, bending effects gradually become dominant, so the green points in the middle relative density regime (between 10% and 20%) closely match theory prediction 3, which considers only bending, as shown in Fig. 10. For high relative densities (over 25%), bending and nodal volume both contribute because of enhanced constraints at the nodes and the increase of nodal volume, while surface effects become negligible. Thus, all blue points are closer to theory prediction 2, which considers both nodal volume and bending. While nodal volume was most important to match the nanolattice stiffness scaling, in both cases surface effects, despite the small strut widths considered, have the least effect on the observed scaling behavior with increasing relative density.

From the analysis of nanolattice stiffness, we found that due to the small aspect ratios of the struts and stronger kinematic constraints at the nodes, the effects of nodal volume and bending have a significant influence compared with ideal octet-truss lattices. Similarly, these effects also impact the yield strength of nanolattices. However, what should be empha-
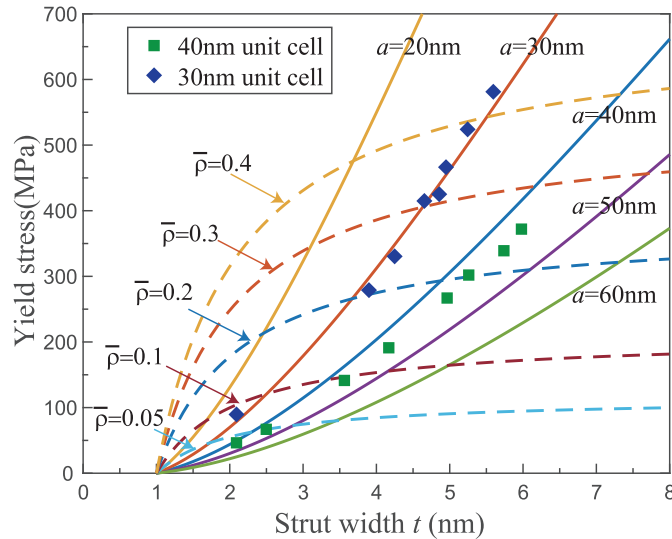
Fig. 11. Yield strength of nanolattices as a function of strut width (dashed lines) and length of unit cell (solid lines) from theory prediction 1 and MD simulations (solid points).

sized is that the rigid joint of the node generates bending moment during compression of nanolattices. Bending moment is first order quantity of axial force, while shear force is second order quantity, which means bending moment is a critical factor decreasing the yield strength of nanolattices. As is shown in Fig. 9, due to bending moment given by Eq. (16), yielding areas are distributed at or near the nodes in the nanolattices, and partial dislocations nucleate and propagate from these areas where compressive stress is maximum in theory analysis. This also explains why most of deformation is localized to the nodes during previous experimental studies of the compression of alumina nanolattices and meso-lattices (Gu and Greer, 2015; Meza et al., 2014). For previously studied octet-truss lattices, nodal connectivity is assumed to be pin-jointed, where their nodes cannot form bending moment during compression, so bending effects are negligible (Deshpande et al., 2001a; Dong et al., 2015). Therefore, our analytic studies demonstrate that reducing the nodal constraint in an octet truss lattice is a feasible approach to enhancing the scaling of strength with density.

Moreover, surface effects have been established to play a key role on the yield strength and mechanisms of individual nanostructures like nanowires (Park et al., 2009, 2006; Weinberger and Cai, 2012). Compared to individual nanowires, however, we find that surface effects have a smaller influence on nanolattices. This is because surface effects compete with bending and nodal volume effects, all of which depend nonlinearly with the nanolattice relative density as discussed above, and shown in Fig. 10. Thus, while surface effects do improve the accuracy of the theoretical models, particularly at lower relative densities, they are not the dominant effect in governing the mechanics of nanolattices.

4.4. Lightweight and strong nanolattices

To compare the yield strength of the Cu nanolattices with other, macroscale nanolattices and other metallic engineering materials, we plot them together on the material property chart in Fig. 12, which shows the density dependent yield strength for existing materials (Ashby, 2011) and other space filling lattice structures, including alumina nanolattices (Meza et al., 2014), Ti-6Al-4V octet-truss lattice(Dong et al., 2015) and Cu meso-lattices (Gu and Greer, 2015). The strengths of both foams and lattices scale with those of the materials from which they are made (Ashby, 2011; Fleck et al., 2010).

As shown in Fig. 12, Cu nanolattices provide higher strength at a lower density compared with Cu meso-lattices, and are about an order of magnitude stronger for the same relative density, which marks a new entry in the high-strength lightweight material parameter space. Compared with meso-lattices, Cu nanolattices have smaller length scales and lower densities but provide higher strength, which exemplifies the well-known "smaller is stronger" effect (Dou and Derby, 2009; Uchic et al., 2004). While we have performed comparison with existing experimental studies, there are clearly differences between the MD simulations performed in this work and those experimental studies. First, the strain rates in the MD simulations are significantly higher than in experiment, which may lead to higher yield stresses in the simulations as compared to those expected at experimental strain rates (Zhu et al., 2008). Furthermore, the struts in our nanolattices are defect free and pristine, whereas in the experimental study of meso-lattices by Gu *et al.* (Gu and Greer, 2015), the microstructure analysis revealed that substantial regions within the meso-lattices consisted of grain and twin boundaries, which leads to different strengthening mechanisms as compared to the defect-free and pristine struts that are considered in the present MD simulations. Therefore, there are both simulation artifacts (higher strain rates), as well as real structural and size effects (smaller, defect-free struts in nanolattices compared to larger struts with significant microstructure in meso-lattices) that
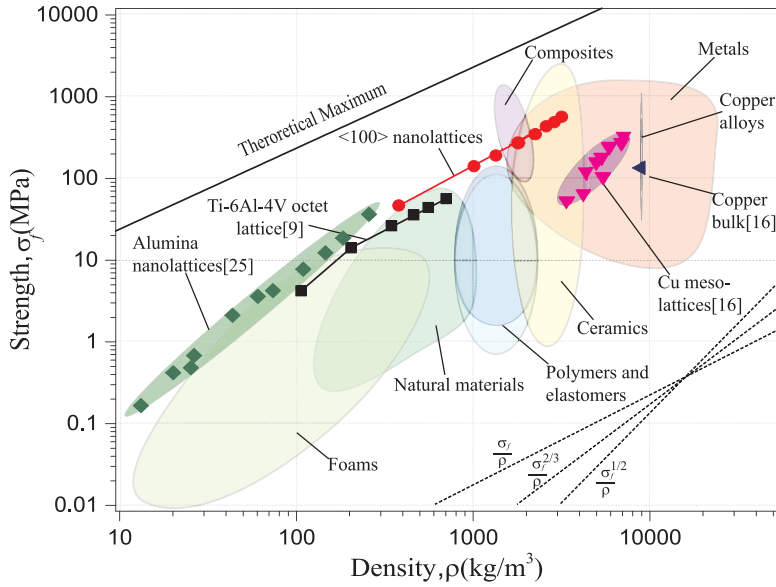
Fig. 12. Material property chart comparing material compressive strength against density. The simulation data and linear fitting of strength for <100> nanolattices has been included for comparison with other octet-truss lattice materials.

contribute to the higher strength seen in the present work as compared to previously studied metallic meso-lattices(Greer and De Hosson, 2011; Gu and Greer, 2015).

Furthermore, fitting the MD simulations by the functional form $\sigma_y \propto \sigma_{ys} \bar{\rho}^m$ (Fleck et al., 2010; Gibson and Ashby, 1999), we obtain the exponent $m = 1.17$, which is slightly higher than ideal octet-truss lattice ($m = 1$) (Deshpande et al., 2001b) and solid HDDA ($m = 1.1$) (Zheng et al., 2014), but lower bending-dominated structures ($m = 3/2$) (Fleck et al., 2010; Gibson and Ashby, 1999) and hollow-tube alumina nanolattices ($m = 1.76$) (Meza et al., 2014). Our scaling is slightly different than the analytic prediction for ideal stretching-dominated structures. This deviation can be explained by Eq. (18), which can be expanded as:

$$\sigma_y \approx 2\sqrt{2}\sigma_{ys}\left(\frac{t}{l}\right)^2\left[1 - \beta\left(\frac{t}{l}\right) + \left(\alpha - \frac{\beta}{2} + \beta^2\right)\left(\frac{t}{l}\right)^2 + \left(\alpha - \frac{\beta}{4} - \alpha\beta + \beta^2 - \beta^3\right)\left(\frac{t}{l}\right)^3\right] \quad (19)$$

where $\alpha = K_T(\lambda_1 + \lambda_2)$, and $\beta = 6\lambda$. Eq. (19) demonstrates that the principle part of Eq. (18) is the same with Eq. (4), which means our nanolattices are still stretching-dominated, so the exponent m should be lower than 3/2. Besides, the contribution of bending effects reduces the exponent m due to the modification of negative (t/l). If we ignore the surface effects and fit theory prediction 2 (which includes bending and nodal volume) with a power law, we find $m = 0.986$, while $m = 1.17$ if theory prediction 4 (only considering nodal volume) is fitted by power law. However, if surface effects are considered and theory prediction 1 is fitted by power law, $m = 1.16$. This result is close to MD simulations, which means bending effects decrease the scaling exponent. Nevertheless, octet-truss nanolattices are mainly stretching-dominated and are simultaneously lightweight and strong, while outperforming bulk copper and copper meso-lattices by reaching a previously unexplored property range in the Ashby plot in Fig. 12.

5. Conclusion

In summary, we performed MD simulations in conjunction with the development of analytic models to study the compressive mechanical properties of octet-truss Cu nanolattices. Significant property enhancements as compared to bulk Cu and Cu meso-lattices were observed, where the strength of nanolattices with high relative density were larger than that of bulk Cu, while nanolattices achieved superior yield strengths with lower relative densities as compared to meso-lattices.

We modified the classical octet truss model to account for nodal volume, bending, and surface effects on the mechanical properties of the nanowire struts. The analytic models were found to be in good agreement with the MD simulation results. These enabled new insights into the mechanisms governing the strength and stiffness scaling of the nanolattices, where nodal volume is the key factor governing the stiffness scaling, while bending dominates the strength scaling.

Perhaps most surprisingly, surface effects, which have previously been shown to cause significant changes in both the elastic and inelastic behavior and properties of individual nanowires, have a smaller impact on the stiffness and strength scaling of nanolattices. This is because, unlike for individual nanowires, the mechanical response of the nanowire struts that form the nanolattice structure is also a function of bending and nodal volume effects, all of which depend nonlinearly on the nanolattice relative density.

Overall, this work demonstrates the promise of nanoscale cellular materials for accessing previously untapped regimes of mechanical performance by simultaneously achieving high strength and low density.

Acknowledgments

References

Ashby, M.F., 2011. Materials Selection in Mechanical Design, fourth ed.

Bauer, J., Schroer, A., Schwaiger, R., Kraft, O., 2016. Approaching theoretical strength in glassy carbon nanolattices. Nat. Mater 15, 438–443.

Boyer, R.D., Li, J., Ogata, S., Yip, S., 2004. Analysis of shear deformations in Al and Cu: empirical potentials versus density functional theory. Model. Simul. Mater. Sci. Eng. 12, 1017.

Cao, A., Ma, E., 2008. Sample shape and temperature strongly influence the yield strength of metallic nanopillars. Acta Mater. 56, 4816–4828.

Deshpande, V.S., Ashby, M.F., Fleck, N.A., 2001a. Foam topology: bending versus stretching dominated architectures. Acta Mater. 49, 1035–1040.

Deshpande, V.S., Fleck, N.A., Ashby, M.F., 2001b. Effective properties of the octet-truss lattice material. J. Mech. Phys. Solids 49, 1747–1769.

Diao, J., Gall, K., Dunn, M.L., 2004. Yield strength asymmetry in metal nanowires. Nano Lett. 4, 1863–1867.

Dingreville, R., Qu, J., 2005. Surface free energy and its effect on the elastic behavior of nano-sized particles, wires and films. J. Mech. Phys. Solids 53, 1827–1854.

Dong, L., Deshpande, V., Wadley, H., 2015. Mechanical response of Ti–6Al–4V octet-truss lattice structures. Int. J. Solids Struct. 60-61, 107–124.

Dou, R., Derby, B., 2009. A universal scaling law for the strength of metal micropillars and nanowires. Scr. Mater. 61, 524–527.

Feng, X.-Q., Xia, R., Li, X., Li, B., 2009. Surface effects on the elastic modulus of nanoporous materials. Appl. Phys. Lett. 94, 011916.

Finnegan, K., Kooistra, G., Wadley, H.N.G., Deshpande, V.S., 2007. The compressive response of carbon fiber composite pyramidal truss sandwich cores. Int. J. Mater. Res 98, 1264–1272.

Fleck, N.A., Deshpande, V.S., Ashby, M.F., 2010. Micro-architectured materials: past, present and future. In: Proceedings of the Royal Society A: Mathematical, Physical and Engineering Sciences, 466, pp. 2495–2516.

Gibson, L.J., Ashby, M.F.X., 1999. Cellular Solids: Structure and Properties. Cambridge university press.

Greer, J.R., De Hosson, J.T.M., 2011. Plasticity in small-sized metallic systems: Intrinsic versus extrinsic size effect. Prog. Mater Sci. 56, 654–724.

Gu, X.W., Greer, J.R., 2015. Ultra-strong architected Cu meso-lattices. Extreme Mech. Lett. 2, 7–14.

He, J., Lilley, C.M., 2008. Surface effect on the elastic behavior of static bending nanowires. Nano Lett. 8, 1798–1802.

Hodge, A.M., Biener, J., Hayes, J.R., Bythrow, P.M., Volkert, C.A., Hamza, A.V., 2007. Scaling equation for yield strength of nanoporous open-cell foams. Acta Mater. 55, 1343–1349.

Hutchinson, J.R., 2001. Shear coefficients for Timoshenko beam theory. J. Appl. Mech. 68, 87–92.

Jang, D., Meza, L.R., Greer, F., Greer, J.R., 2013. Fabrication and deformation of three-dimensional hollow ceramic nanostructures. Nat. Mater. 12, 893–898.

Jennings, A.T., Burek, M.J., Greer, J.R., 2010. Microstructure versus size: mechanical properties of electroplated single crystalline Cu nanopillars. Phys. Rev. Lett. 104, 135503.

Kelchner, C.L., Plimpton, S.J., Hamilton, J.C., 1998. Dislocation nucleation and defect structure during surface indentation. Phys. Rev. B 58, 11085.

Lee, S.W., Jafary-Zadeh, M., Chen, D.Z., Zhang, Y.W., Greer, J.R., 2015. Size effect suppresses brittle failure in hollow Cu60Zr40 metallic glass nanolattices deformed at cryogenic temperatures. Nano. Lett. 15, 5673–5681.

Liang, H., Upmanyu, M., Huang, H., 2005. Size-dependent elasticity of nanowires: nonlinear effects. Phys. Rev. B 71, 241403.

Meyers, M.A., Chawla, K.K., 2009. Mechanical Behavior of Materials. Cambridge university press Cambridge.

Meza, L.R., Das, S., Greer, J.R., 2014. Strong, lightweight, and recoverable three-dimensional ceramic nanolattices. Science 345, 1322–1326.

Meza, L.R., Zelhofer, A.J., Clarke, N., Mateos, A.J., Kochmann, D.M., Greer, J.R., 2015. Resilient 3D hierarchical architected metamaterials. In: Proceedings of the National Academy of Sciences, 112, pp. 11502–11507.

Miller, R.E., Shenoy, V.B., 2000. Size-dependent elastic properties of nanosized structural elements. Nanotechnology 11, 139.

Mishin, Y., Mehl, M.J., Papaconstantopoulos, D.A., Voter, A.F., Kress, J.D., 2001. Structural stability and lattice defects in copper: Ab initio, tight-binding, and embedded-atom calculations. Phys. Rev. B 63, 224106.

Montemayor, L.C., Greer, J.R., 2015. Mechanical response of hollow metallic nanolattices: combining structural and material size effects. J. Appl. Mech. 82, 071012.

Moongkhamklang, P., Deshpande, V.S., Wadley, H.N.G., 2010. The compressive and shear response of titanium matrix composite lattice structures. Acta Mater. 58, 2822–2835.

Park, H.S., Cai, W., Espinosa, H.D., Huang, H., 2009. Mechanics of crystalline nanowires. MRS Bull. 34, 178–183.

Park, H.S., Gall, K., Zimmerman, J.A., 2006. Deformation of FCC nanowires by twinning and slip. J. Mech. Phys. Solids 54, 1862–1881.

Park, H.S., Klein, P.A., 2008. Surface stress effects on the resonant properties of metal nanowires: the importance of finite deformation kinematics and the impact of the residual surface stress. J. Mech. Phys. Solids 56, 3144–3166.

Plimpton, S., 1995. Fast parallel algorithms for short-range molecular dynamics. J. Comput. Phys. 117, 1–19.

Schaedler, T.A., Carter, W.B., 2016. Architected cellular materials. Annu. Rev. Mater. Res.

Schaedler, T.A., Jacobsen, A.J., Torrents, A., Sorensen, A.E., Lian, J., Greer, J.R., Valdevit, L., Carter, W.B., 2011. Ultralight metallic microlattices. Science 334, 962–965.

Shenoy, V.B., 2005. Atomistic calculations of elastic properties of metallic fcc crystal surfaces. Phys. Rev. B 71.

Stukowski, A., 2009. Visualization and analysis of atomistic simulation data with OVITO–the Open Visualization Tool. Model. Simul. Mater. Sci. Eng. 18, 015012.

Stukowski, A., Bulatov, V.V., Arsenlis, A., 2012. Automated identification and indexing of dislocations in crystal interfaces. Model. Simul. Mater. Sci. Eng. 20, 085007.

Sun, Z.H., Wang, X.X., Wu, H.A., 2008. Surface relaxation effect on the distributions of energy and bulk stresses in the vicinity of Cu surface: an embedded-atom method study. J. Appl. Phys. 104, 033501.

Timoshenko, S.P., Goodier, J.N., 1970. Theory of Elasticity, third ed. MacGraw Hill International Book.

Tschopp, M.A., McDowell, D.L., 2008. Influence of single crystal orientation on homogeneous dislocation nucleation under uniaxial loading. J. Mech. Phys. Solids 56, 1806–1830.

Uchic, M.D., Dimiduk, D.M., Florando, J.N., Nix, W.D., 2004. Sample dimensions influence strength and crystal plasticity. Science 305, 986–989.

Wang, G.-F., Feng, X.-Q., 2009. Surface effects on buckling of nanowires under uniaxial compression. Appl. Phys. Lett. 94, 141913.

Weinberger, C.R., Cai, W., 2012. Plasticity of metal nanowires. J. Mater. Chem. 22, 3277.

Xia, R., Li, X., Qin, Q., Liu, J., Feng, X.Q., 2011. Surface effects on the mechanical properties of nanoporous materials. Nanotechnology 22, 265714.

Yang, Z., Lu, Z., Zhao, Y.-P., 2009. Atomistic simulation on size-dependent yield strength and defects evolution of metal nanowires. Comput. Mater. Sci. 46, 142–150.

Zhang, W., Wang, T., Chen, X., 2008. Effect of surface stress on the asymmetric yield strength of nanowires. J. Appl. Phys. 103, 123527.

Zheng, X., Lee, H., Weisgraber, T.H., Shusteff, M., DeOtte, J., Duoss, E.B., Kuntz, J.D., Biener, M.M., Ge, Q., Jackson, J.A., 2014. Ultralight, ultrastiff mechanical metamaterials. Science 344, 1373–1377.

Zheng, X., Smith, W., Jackson, J., Moran, B., Cui, H., Chen, D., Ye, J., Fang, N., Rodriguez, N., Weisgraber, T., 2016. Multiscale metallic metamaterials. Nat. Mater 15, 1100–1106.

Zhou, M., 2003. A new look at the atomic level virial stress: on continuum-molecular system equivalence. Proc. R. Soc. London A 459, 2347–2392.

Zhu, T., Li, J., Samanta, A., Leach, A., Gall, K., 2008. Temperature and strain-rate dependence of surface dislocation nucleation. Phys. Rev. Lett. 100, 025502.